

MICROBIOLOGY

Supercharged precision killers: Genetically engineered biomimetic drugs of screened metalloantibiotics against *Acinetobacter baumannii*

Xianyuan Wei^{1†}, Bin Xue^{1,2†}, Shuangchen Ruan^{2†}, Jintong Guo¹, Yujing Huang¹, Xiaorui Geng¹, Dan Wang³, Cangtao Zhou², Jun Zheng¹, Zhen Yuan^{1*}

To eliminate multidrug-resistant bacteria of *Acinetobacter baumannii*, we screened 1100 Food and Drug Administration–approved small molecule drugs and accessed the broxyquinoline (Bq) efficacy in combination with various metal ions. Antibacterial tests demonstrated that the prepared Zn(Bq)₂ complex showed ultralow minimum inhibitory concentration of ~0.21 micrograms per milliliter with no resistance after 30 passages. We then constructed the nano zeolitic imidazolate framework-8 (ZIF-8) as a drug carrier of Zn(Bq)₂ and also incorporated the photosensitizer chlorin e6 (Ce6) to trace and boost the antibacterial effect. To further ensure the stable and targeted delivery, we genetically engineered outer membrane vesicles (OMVs) with the ability to selectively target *A. baumannii*. By coating the ZnBq/Ce6@ZIF-8 core with these OMV, the resulted drug (ZnBq/Ce6@ZIF-8@OMV) exhibited exceptional killing efficacy (>99.9999999%) of *A. baumannii*. In addition, *in vitro* and *in vivo* tests were also respectively carried out to inspect the remarkable efficacy of this previously unknown nanodrug in eradicating *A. baumannii* infections, including biofilms and meningitis.

INTRODUCTION

Acinetobacter baumannii is a type of multidrug-resistant bacteria (MDRB) that has developed resistance to all available antibacterial drugs (1–7). This bacterium primarily causes hospital-acquired infections, making it an opportunistic pathogen with widespread prevalence (8, 9). These infections can result in severe or even fatal diseases, such as pneumonia, urethritis, bloodstream infections, and meningitis, with mortality rates reaching up to 60% (10, 11). The World Health Organization (WHO) has classified *A. baumannii* as a “critical priority pathogen” due to its resistance to existing treatments, emphasizing the urgent need for new treatment strategies (12–14). Therefore, it is essential to develop innovative and effective antibacterial agents to combat *A. baumannii*. Presently, the antibiotics being developed clinically predominantly belong to existing categories and are often analogs of already-known drugs (15). Although these structurally similar antibacterial agents might meet short-term clinical requirements, they do not provide a long-term solution to the problem of drug resistance. As a result, traditional organic antibacterial agents are unable to effectively supplement the diminishing antibacterial pipeline.

Unlike traditional organic small molecules, metal complexes have a distinct three-dimensional arrangement around one or more metal centers, facilitated by multiple ligands. This unique structure allows metal complexes to exhibit greater stereochemical variability, earning them the term “metalloantibiotics” (16–18). The three-dimensional structure of metal complexes confers superior targeting binding ability and reduces the risk of off-target interactions associated with chiral centers in organic molecules (19, 20). Besides,

the intricate three-dimensional structure hinders the efflux pumps responsible for eliminating Gram-negative bacteria (21, 22). As a result, metal complexes typically exhibit stronger antibacterial effects as compared to their parent ligands. However, only several types of metal complexes that can effectively eradicate MDRB are inspected. To date, novel metal complexes that can effectively kill the highly resistant *A. baumannii* have not yet been found.

In addition to the ongoing development of new antibacterial drugs based on metal complexes, there is a lack of investigations focusing on enhancing their targeting and delivery capabilities. Although a number of metal complexes are designed with the addition of hydrophobic groups to facilitate penetration of bacterial membranes (23), this hydrophobicity poses challenges for *in vivo* drug transport. Furthermore, apart from water solubility, highly active metal complexes might undergo ligand exchange reactions when exposed to different biological environments (24, 25), causing the loss of their antibacterial activity. Therefore, it is crucial to protect the stable structure of metal complexes and ensure efficient delivery to the targeted bacterial sites.

Recent natural and synthetic cell membrane-coated nanoparticles, also known as “biomimetic nanoparticles,” have shown the potential for killing MDRB and eradicating biofilms (26–29). The cell membrane-camouflaged biomimetic nanoparticles consist of a nanoparticle core and an outer cell membrane shell (30, 31). In particular, the outer membrane is derived from an appropriate cell membrane type, serving to prolong blood circulation time, deliver drugs to the targeted sites, and perform disease treatments. Various categories of cell membranes, including red blood cell membranes, platelet membranes, macrophage membranes, bacterial membranes, and bacterial outer membrane vesicles (OMVs), have been extracted to carry out targeted antibacterial and anticancer treatments (32, 33). However, these membrane structures normally lack the specific targeting ability to target MDRB such as *A. baumannii*. By contrast, recent advances in genetic engineering made it possible to modify natural cell membrane structures to produce a more targeted cell membrane. For example, genetically engineered *Escherichia coli* was

Copyright © 2024 The Authors, some rights reserved; exclusive licensee American Association for the Advancement of Science. No claim to original U.S. Government Works. Distributed under a Creative Commons Attribution NonCommercial License 4.0 (CC BY-NC).

¹Centre for Cognitive and Brain Sciences and Ministry of Education Frontiers Science Center for Precision Oncology, University of Macau, Macau SAR, China. ²Shenzhen Key Laboratory of Ultraintense Laser and Advanced Material Technology, Center for Intense Laser Application Technology and College of Engineering Physics, Shenzhen Technology University, Shenzhen 518118, China. ³The Hong Kong Polytechnic University Shenzhen Research Institute, Shenzhen 518000, China.

*Corresponding author. Email: zhenyuan@um.edu.mo

†These authors contributed equally to this work.

able to yield OMV with specific protein expression for tumor-targeting therapy (34–36). It is also possible to use gene engineering technology to target MDRB with natural membrane structures and to develop highly biocompatible and bacterial-specific targeting strategies to effectively kill MDRB.

In this study, we have achieved successful genetic engineering of OMV nanodrugs, enabling them as a targeted drug delivery system for eradicating MDRB like *A. baumannii* (Fig. 1A). By genetically modifying an msbB mutant *E. coli* strain (MG1655) and fusing the ClyA coding region with a targeted antibody fragment (37), we were able to produce OMVs that selectively target *A. baumannii*. In addition, we also constructed highly efficient killing core nanostructures to combat *A. baumannii* in conjunction with the targeted delivery system. In particular, according to our screening process involving over 1100 small molecules and various types and concentrations of metal ions, we successfully identified a metal complex, Zn(Bq)₂, which was able to effectively eradicate *A. baumannii*. To ensure the stability and efficient transport of Zn(Bq)₂, we used zeolitic imidazolate framework-8 (ZIF-8) as a drug carrier platform. ZIF-8 was chosen because of its exceptional characteristics such as ultrahigh porosity, large specific surface area, pH-induced biodegradability, and excellent biocompatibility (38, 39). Furthermore, nanoscale ZIF-8 can prevent drug extravasation and renal clearance during transport. To enhance antibacterial efficacy and facilitate visualization and monitoring of drug transport and bacterial uptake, we incorporated the photosensitizer molecule chlorin e6 (Ce6) into ZIF-8, resulting in the formation of ZnBq/Ce6@ZIF-8 nanostructures. Last, we coated the genetically engineered OMV onto the surface of the ZnBq/Ce6@ZIF-8 core, culminating in the development of a novel nanodrug (ZnBq/Ce6@ZIF-8@OMV) with targeted killing ability against *A. baumannii*. To inspect the potential of these new drugs for the treatment of *A. baumannii*-induced meningitis,

we conducted both in vitro and in vivo tests (Fig. 1B). This pilot work paves the way for the development of novel targeted drugs in combating MDRB.

RESULTS

Screen and antibacterial properties of Zn(Bq)₂

To effectively combat the antibiotic-resistant *A. baumannii*, we first screened and identified the compound of Zn(Bq)₂. In particular, over 1100 compounds (40 μM) from a library of Food and Drug Administration (FDA)-approved antimicrobial compounds. Were incubated with *A. baumannii* ATCC 19606 in a 96-well plate, in which their antibacterial efficacy was accessed by measuring the bacterial growth at 600 nm after 24 hours of incubation. It was found that 11 compounds with an OD₆₀₀ (optical density at 600 nm) less than 0.1 were detected as potential antibacterial agents for the first-round screening (Fig. 2A). However, after excluding compounds that have been used in infection therapy, only four drugs, namely, lomerizine HCl, methacycline hydrochloride, dibucaine HCl, and broxyquinoline (Bq), were selected for further screening. Meanwhile, a minimum inhibitory concentration (MIC) test was performed (Fig. 2B), showing that Bq exhibited the strongest antimicrobial activity among the four selected compounds (about 2 μg/ml). Bq was very effective in eliminating MDR *A. baumannii* strains, including *A. baumannii* ATCC 19606 (Fig. 2C), *A. baumannii* BAA-1800 (Fig. 2D), and *A. baumannii* ATCC 17978 (Fig. 2E) at a low concentration of 5 μg/ml.

Notably, the identified Bq compound has O- and N-donor groups (Fig. 2F) that might chelate metal ions, which may result in a synergistic effect on killing MDRB. Checkboard experiments (Fig. 2G) revealed the antibacterial effect of Bq in combination with other representative metal ions in a physiological environment, such as Fe(II),

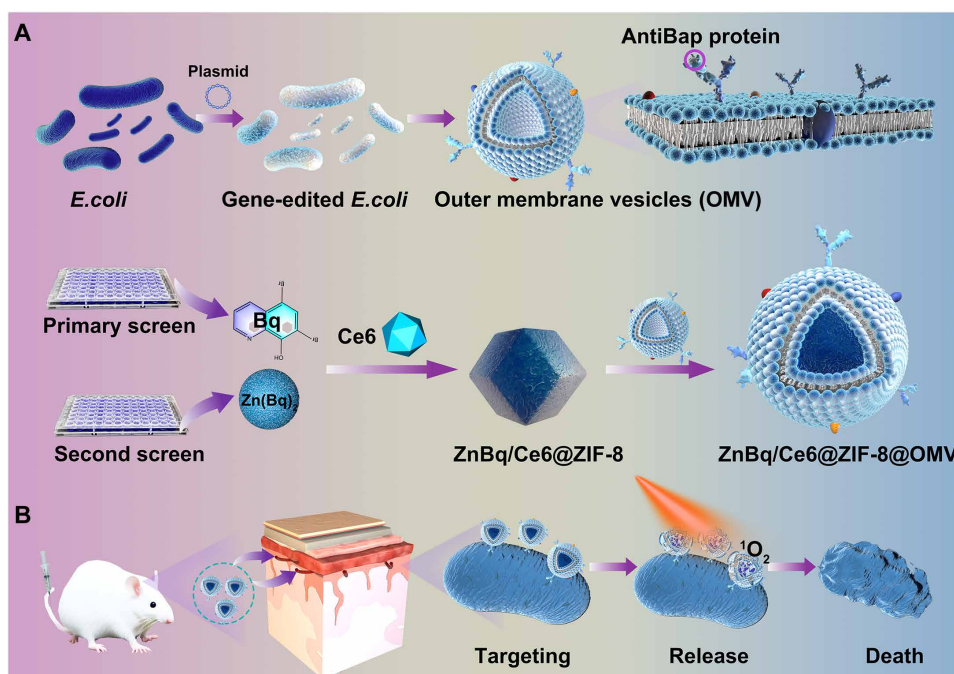


Fig. 1. Schematic of construction of ZnBq/Ce6@ZIF-8@OMV with antibacterial activity. (A) Synthesis process of ZnBq/Ce6@ZIF-8@OMV. (B) Schematic of the antibacterial performance of ZnBq/Ce6@ZIF-8@OMV for targeted treatment of MDR *A. baumannii*-induced meningitis.

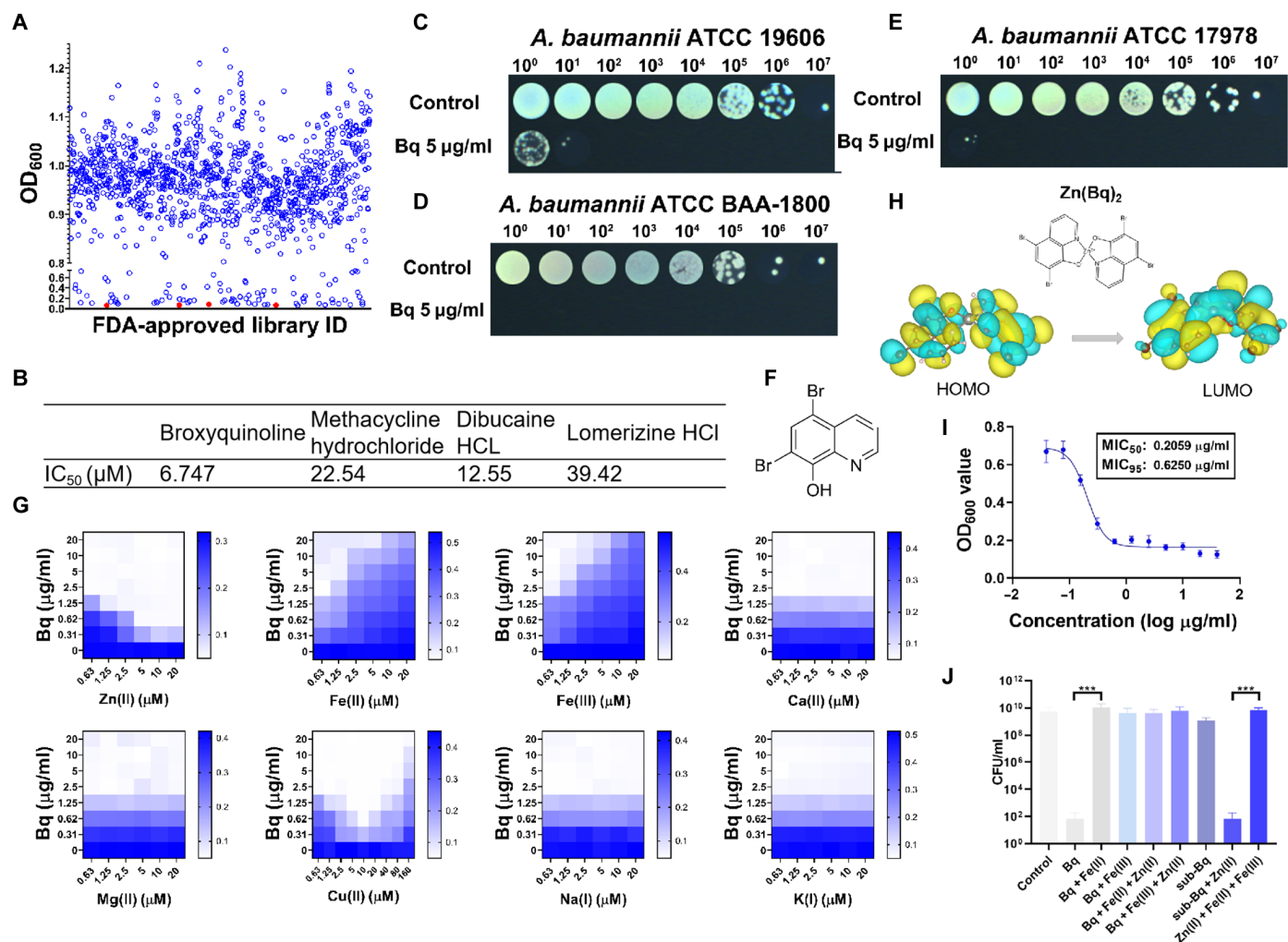


Fig. 2. Bacterial killing ability of ZnBq/Ce6@ZIF-8@OMV against multidrug-resistant *A. baumannii*. (A) Dot plot diagram representing the entire screening data from 1100 compounds to identify antimicrobial activity for *A. baumannii*. The red dotted line depicts the boundary of the target used to identify the components that cause the bacteria growth of $OD_{600} < 0.1$. The red dots under the red dotted line represent the selected drugs: lomerizine HCl, methacycline hydrochloride, dibucaine HCL, and broxyquinoline (Bq). (B) IC₅₀ (median inhibitory concentration) values of the four selected drugs. Various concentrations ($10^0 \sim 10^7$) of *A. baumannii* ATCC 19606 (C), *A. baumannii* BAA-1800 (D), and *A. baumannii* ATCC 17978 (E) grown on agar plates with or without Bq (5 μg/ml). (F) The molecular structural formula of Bq. (G) Checkerboard plots for the antibacterial activity of Bq together with various metal ions. (H) Partial charge density plot of the highest occupied molecular orbital (HOMO) and lowest unoccupied molecular orbital (LUMO) levels of Zn(Bq)₂. (I) Dose-dependent growth inhibition *A. baumannii* by Zn(Bq)₂; data are expressed as the means ± SD of three individual experiments. (J) Antibacterial activity through orthogonal experiment under different conditions. Bq: (5 μg/ml), sub-Bq: 1 μg/ml, Zn(II): 5 μM, Fe(II): 5 μM, Fe(III): 5 μM.

Fe(III), Zn(II), Cu(II), Na(I), K(I), Mg(II), and Ca(II) ions. According to the calculation of the fractional inhibitory concentration index (FICI), we found that Fe(II) and Fe(III) ions were antagonistic with Bq, whereas Zn(II) ions exhibited a synergistic antibacterial effect with Bq. During the FICI testing process, we found that after incubation of zinc ions and Bq, the solution immediately produced a yellow color (fig. S1). We further infer this antagonism or synergism effect might be due to the coordination ability of Bq with metal ions. It is well known that the absorption of metal complexes in the visible region is significantly enhanced compared to that of the parent ligand molecules which is primarily attributed to the occurrence of ligand-to-metal or metal-to-ligand charge transfer processes (as exemplified in Fig. 2H, calculation results indicating ligand-to-Zn charge transfer). Hence, the coordination of Bq with metal ions can

be conveniently observed via absorption spectra. In our study, we observed a clear correlation between the antibacterial efficiency and the coordination of Bq with metal ions. Notably, metal ions such as Ca(II), Mg(II), Na(I), and K(I), which have minimal impact on the antibacterial efficiency of Bq (Fig. 2G), also do not induce any significant changes in the absorption characteristics of Bq (fig. S2). By contrast, the addition of Zn(II), Cu(II), Fe(II), and Fe(III) ions to Bq resulted in a significant change in Bq absorption (fig. S3), indicating that Bq was able to coordinate with these metal ions. The distinct shifts in vibration peak positions detected by Fourier transform infrared data also illustrated the capability of the coordination of Bq with these metal ions (fig. S4). In addition, our experimental results (figs. S5 to S8) and theoretical calculations (figs. S9 to S13 and table S1) demonstrated that $Fe(III) \approx Fe(II) > Cu(II) \approx Zn(II)$ in terms

of coordination strength with Bq. The discovery of the coordination between Bq and metal ions resulting in the formation of a complex such as $\text{Zn}(\text{Bq})_2$ dates back several decades (40, 41). Initially, $\text{Zn}(\text{Bq})_2$ found its primary application in electroluminescent materials (42). However, the $\text{Zn}(\text{Bq})_2$ generated in this study exhibits exceptional antibacterial efficacy, with a calculated 50% inhibition rate of MIC value as low as 0.21 $\mu\text{g}/\text{ml}$ (Fig. 2I). Unexpectedly, the inclusion of iron ions (Fig. 2, G and J) and high concentration copper ions (Fig. 2G and fig. S14) actually diminished the antibacterial potential of Bq. On the basis of the varying coordination abilities of these metal ions with Bq, we postulate that the observed antibacterial efficacy might be closely linked to the coordination interactions between metal ions and Bq. Here, we found that this metal complex $\text{Zn}(\text{Bq})_2$ exhibited excellent antibacterial properties. Moreover, we further found that $\text{Zn}(\text{Bq})_2$ showed good structural stability in most media (fig. S15).

Synthesis and characterization of $\text{ZnBq}/\text{Ce6}@ZIF-8@OMV$

We constructed the bioengineered outer membrane vesicles as the targeted transport part. To produce the OMV, we engineered *E. coli* to express the desired targeted antibody protein and then coated the extracted OMV onto $\text{ZnBq}/\text{Ce6}@ZIF-8$ to produce $\text{ZnBq}/\text{Ce6}@ZIF-8@OMV$. More specifically, gene-editing technology was used to construct the plasmid pBAD_{clyA}-antiBap, which expresses the fused targeted protein ClyA-antiBap and an in-frame deletion mutant of ΔmsbB in *E. coli* MG1655 (Fig. 3, A and B). The mutant colonies of msbB exhibit a significant reduction in length, measuring 642 base pairs (bp) shorter compared to the wild type (Fig. 3C). The knockout of msbB gene for the present study was derived from an under-age type of penta-acylated lipopolysaccharide OMV, which is associated with reduced endotoxicity and side effects (43, 44). The successful expression of ClyA-antiBap protein in ΔmsbB (pBAD_{clyA}-antiBap) strain under L-arabinose induce was demonstrated by using SDS page (fig. S16) and Western blot (Fig. 3D), with the predicted protein weight of 50.4 kDa.

For the core part, the encapsulation procedure for $\text{Zn}(\text{Bq})_2$ and Ce6 in ZIF-8 was conducted using the in situ synthesis method (see experimental section for details). First, the Bq ligands and Ce6 were added to the ZIF-8 precursors, and then the nanodrugs were prepared following a modified ZIF-8 synthesis route. Traditional methods involve mixing and stirring presynthesized large pore size Metal-Organic Framework (MOF) with metal complexes to obtain MOF-loaded metal complexes (45, 46). However, this method yielded low drug loading in our system. Fortunately, we found that Bq and Zn ions can be readily converted to $\text{Zn}(\text{Bq})_2$ (fig. S17), where the colorless Bq turns into yellow $\text{Zn}(\text{Bq})_2$, with a conversion process taking less than 10 s (fig. S18). Exploiting this property, Bq was added to the ZIF-8 precursor solution, facilitating the rapid formation of $\text{Zn}(\text{Bq})_2$ (fig. S19). Subsequently, the in situ growth of ZIF-8 ensued, resulting in the efficient loading of $\text{Zn}(\text{Bq})_2$ during synthesis. The produced $\text{ZnBq}/\text{Ce6}@ZIF-8$ nanoparticles were uniformly distributed with an average size of 46 nm, as demonstrated by the representative scanning electron microscopy (SEM) and transmission electron microscopy (TEM) images (Fig. 3, E and F, and fig. S20). In addition, high-angle annular dark-field scanning TEM analysis (Fig. 3G) was performed to confirm the presence of a uniform distribution of C, N, Zn, O, and Br elements of $\text{ZnBq}/\text{Ce6}@ZIF-8$, demonstrating the successful loading of $\text{Zn}(\text{Bq})_2$ and Ce6 into ZIF-8. Furthermore, the elemental composition was quantified

by using energy-dispersive x-ray elements analysis (fig. S21) and x-ray photoelectron spectroscopic (XPS) measurement (fig. S22). The powder x-ray diffraction (PXRD) measurement was also carried out to inspect the crystallinity of the products. The PXRD patterns of $\text{ZnBq}/\text{Ce6}@ZIF-8$ agreed well with the standard Bragg reflections of pure ZIF-8 (Fig. 3H), demonstrating a highly crystalline and zeolite-type structure. In particular, to examine the porosity of $\text{ZnBq}/\text{Ce6}@ZIF-8$, the nitrogen gas absorption-desorption measurements were performed. It was found from Fig. 3I that the surface area of $\text{ZnBq}/\text{Ce6}@ZIF-8$ was 241.7 m^2/g [calculated by using the Brunauer-Emmett-Teller (BET) theory], which was substantially lower than the BET surface area value (1156.6 m^2/g) of pure ZIF-8. Besides, a significant reduction in the Langmuir surface area and t -plot micropore area of $\text{ZnBq}/\text{Ce6}@ZIF-8$ was also detected, as compared to those of pure ZIF-8 (figs. S23 and S24), demonstrating that $\text{Zn}(\text{Bq})_2$ and Ce6 were successfully encapsulated into ZIF-8. The absorption peaks measured by the optical absorption spectra also demonstrated the loading of $\text{Zn}(\text{Bq})_2$ and Ce6 into ZIF-8 (Fig. 3J). The encapsulated rate of $\text{Zn}(\text{Bq})_2$ and Ce6 in ZIF-8 nanoparticles was 1.530 and 0.577 wt %, respectively (fig. S25).

Thus, we extracted endotoxic OMV-antiBap and identified the ClyA-antiBap on the surface of $\text{ZnBq}/\text{Ce6}@ZIF-8$ (figs. S26 and S27). The mixture of fresh OMV and prepared $\text{ZnBq}/\text{Ce6}@ZIF-8$ were repeatedly extruded through the 100-nm membrane by Avanti Mini-Extruder. The mechanical force facilitated the coating of OMV on $\text{ZnBq}/\text{Ce6}@ZIF-8$. The gradually increased size measured by dynamic light scattering (Fig. 3K) and decreased zeta potentials (Fig. 3L) further confirmed the fusion process of $\text{ZnBq}/\text{Ce6}@ZIF-8$ and OMV. The constructed $\text{ZnBq}/\text{Ce6}@ZIF-8@OMV$ had a diameter of around 132 nm, while the zeta potential decreased to approximately the level of OMV. Meanwhile, TEM images clearly demonstrated that $\text{ZnBq}/\text{Ce6}@ZIF-8$ was coated with an outer membrane structure (Fig. 3M). The successful coating was also demonstrated by the SDS page (Fig. 3N) and Western blot (Fig. 3O). The stability of $\text{ZnBq}/\text{Ce6}@ZIF-8@OMV$ in water or physiological medium was excellent (fig. S28), exhibiting the potential for in vivo tests.

In addition to $\text{Zn}(\text{Bq})_2$, we also successfully loaded Ce6, an FDA-approved photosensitizer, into $\text{ZnBq}/\text{Ce6}@ZIF-8@OMV$ for completely eliminating *MDR A. baumannii* strains through Photodynamic Therapy (PDT). We used a chemical probe of 1,3-diphenylisobenzofuran (DPBF) to detect the generation of toxic singlet oxygen ($^1\text{O}_2$) by Ce6. We found that the control groups (drug-only or light irradiation-only) did not show any change in DPBF absorption (fig. S29), whereas under 660-nm light irradiation for 10 min, the DPBF absorption decreased in the $\text{ZnBq}/\text{Ce6}@ZIF-8@OMV$ treatment group (fig. S30), indicating the generation of $^1\text{O}_2$. The generated $^1\text{O}_2$ could destroy the fully coated membrane of $\text{ZnBq}/\text{Ce6}@ZIF-8@OMV$ (fig. S30) and facilitate the release of loaded drugs. It was also found that the release of Ce6 and $\text{Zn}(\text{Bq})_2$ was highly pH-dependent due to the decomposition of the ZIF-8 structure under acidic conditions (fig. S31). The pH-response $\text{ZnBq}/\text{Ce6}@ZIF-8@OMV$ minimized the drug leakage while promoting release in the acidic bacteria-infected tissue microenvironment under laser irradiation. This synergistic strategy offers a promising approach to developing responsive nanocarriers for antibacterial treatment.

In vitro antibacterial properties of $\text{ZnBq}/\text{Ce6}@ZIF-8@OMV$

The antimicrobial efficacy of $\text{ZnBq}/\text{Ce6}@ZIF-8@OMV$ against *A. baumannii* was also assessed in vitro. To visually observe therapeutic

was capable of inhibiting biofilm formation (Fig. 4, D and F). However, at lower doses [containing $\text{Zn}(\text{Bq})_2 \sim 0.44 \mu\text{g}/\text{ml}$], these molecules alone were insufficient to completely inhibit biofilm (Fig. 4E). Comparatively, the $\text{ZnBq}/\text{Ce6@ZIF-8@OMV} + \text{light}$ treatment group exhibited mostly all red signals of dead bacteria inside biofilm (Fig. 4E), whereas the control groups contained a significant amount of green living bacteria. Similarly, the low bacterial count observed in the biofilms tube also demonstrated that $\text{ZnBq}/\text{Ce6@ZIF-8@OMV} + \text{light}$ treatment successfully eradicated the *A. baumannii*-induced biofilms (Fig. 4G). These findings highlight the promising super antimicrobial activity of $\text{ZnBq}/\text{Ce6@ZIF-8@OMV}$ in vitro.

ZnBq/Ce6@ZIF-8@OMV-targeted *A. baumannii* bacteria

To comprehend the underlying antibacterial mechanism, we first determine whether the nanodrugs could effectively target and enter bacteria. To test this, we incubated bacteria with $\text{ZnBq}/\text{Ce6@ZIF-8@OMV}$ and then treated them with Hoechst 33342, a bacterial positioning dye. Since $\text{ZnBq}/\text{Ce6@ZIF-8@OMV}$ exhibited red fluorescence (due to Ce6) and Hoechst 33342 generated blue fluorescence (fig. S32), we were able to observe that colocalization yielded a pink overlap when the images were merged (Fig. 5A). Using the fluorescence intensity profiles for three regions of interest, we found that the red fluorescence intensity profile closely matched the blue

fluorescence intensity profile, with a Pearson's R value of 0.83. This indicates that $\text{ZnBq}/\text{Ce6@ZIF-8@OMV}$ effectively targeted and entered *A. baumannii* bacteria. In contrast, when we tested $\text{ZnBq}/\text{Ce6@ZIF-8}$ without OMV coating, we observed little red fluorescence in the bacteria (Fig. 5B), further supporting the idea that OMV coating is important for targeting. Flow cytometry analysis further illustrated that the OMV-coated nanodrugs were rapidly internalized by bacteria through the bacterial-targeted membrane OMV-antiBap (Fig. 5C). This targeting ability led to faster and more effective bacterial killing ability compared to drugs without targeting ability (Fig. 5D). In addition, we tested the reactive oxygen species (ROS) generation capacity of $\text{ZnBq}/\text{Ce6@ZIF-8@OMV}$ using 2',7'-dichlorodihydrofluorescein diacetate, which detects ROS by emitting green fluorescence when oxidized by ROS (Fig. 5E). We found that the $\text{ZnBq}/\text{Ce6@ZIF-8@OMV}$ group generated a significantly higher level of ROS in *A. baumannii* in response to light irradiation than control groups without the targeted OMV (fig. S33), indicating that targeted OMV help generate ROS inside the bacteria.

Mechanism of ZnBq/Ce6@ZIF-8@OMV to kill *A. baumannii* bacteria

To deepen our understanding of the antibacterial mechanism, we investigated the impact of nanodrugs on bacterial membrane integrity

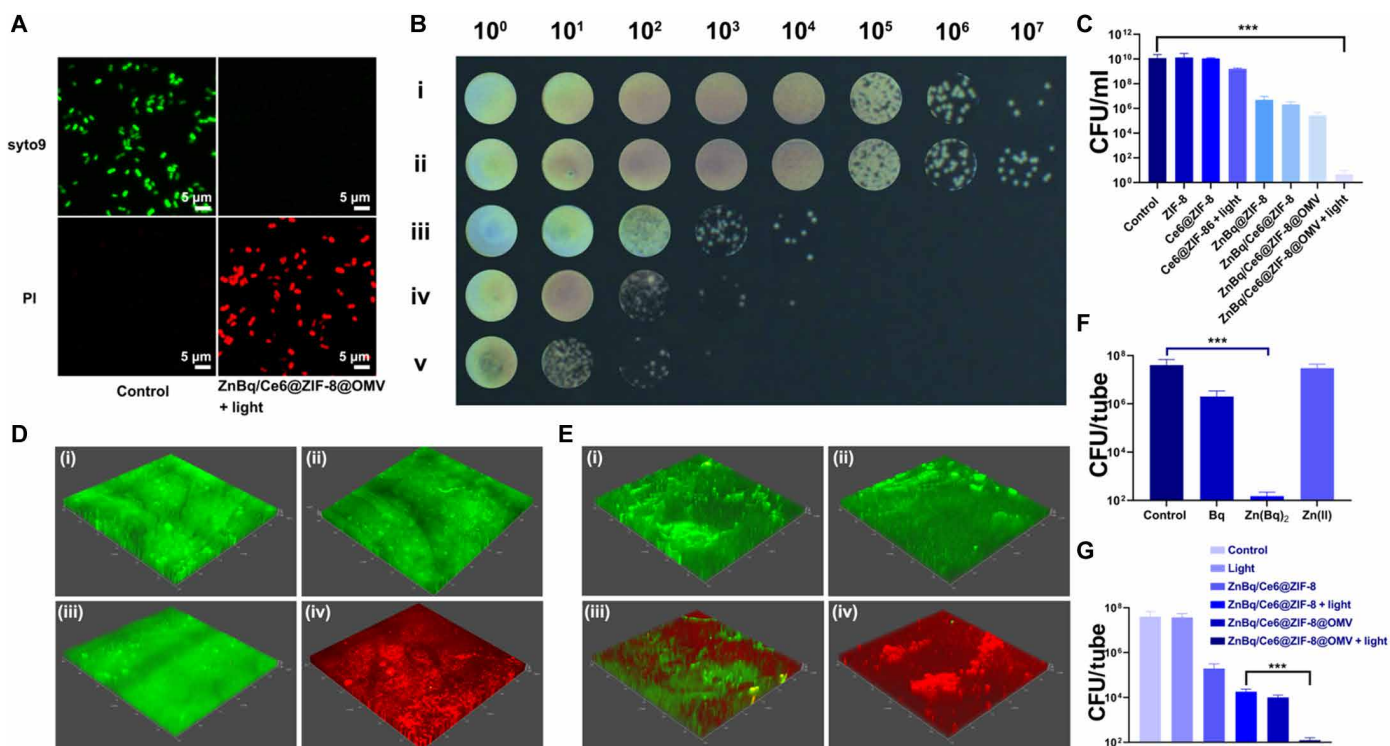


Fig. 4. In vitro antibacterial efficacy of ZnBq/Ce6@ZIF-8@OMV. (A) Detection of live/dead bacteria after different treatments, the live and dead bacteria stained with syto9 (green) and propidium iodide (PI) (red), respectively. $\text{ZnBq}/\text{Ce6@ZIF-8@OMV}$ (40 $\mu\text{g}/\text{ml}$). (B) Representative photos of bacterial colonies on agar plates after 2-hour treatment with (i) phosphate-buffered saline (PBS), (ii) ZIF-8 (40 $\mu\text{g}/\text{ml}$), (iii) $\text{Zn}(\text{Bq})_2$ (1.1 $\mu\text{g}/\text{ml}$), (iv) $\text{ZnBq}/\text{Ce6@ZIF-8}$ (40 $\mu\text{g}/\text{ml}$), and (v) $\text{ZnBq}/\text{Ce6@ZIF-8@OMV}$ (40 $\mu\text{g}/\text{ml}$). (C) Bacterial killing rate after 24-hour treatments for different groups: ZIF-8 (40 $\mu\text{g}/\text{ml}$), Ce6@ZIF-8 (40 $\mu\text{g}/\text{ml}$), $\text{ZnBq}/\text{ZIF-8}$ (40 $\mu\text{g}/\text{ml}$), $\text{ZnBq}/\text{Ce6@ZIF-8}$ (40 $\mu\text{g}/\text{ml}$), $\text{ZnBq}/\text{Ce6@ZIF-8@OMV}$ (40 $\mu\text{g}/\text{ml}$), and $\text{ZnBq}/\text{Ce6@ZIF-8@OMV}$ (40 $\mu\text{g}/\text{ml}$) + light. (D) Antibiofilm activity of (i) control, (ii) Bq (1 $\mu\text{g}/\text{ml}$), (iii) Zn(II) 50 μM , and (iv) $\text{Zn}(\text{Bq})_2$ (1.1 $\mu\text{g}/\text{ml}$). (E) Antibiofilm activity of (i) control, (ii) light, (iii) $\text{ZnBq}/\text{Ce6@ZIF-8@OMV}$ (40 $\mu\text{g}/\text{ml}$, contain $\text{Zn}(\text{Bq})_2 \sim 0.44 \mu\text{g}/\text{ml}$), and (iv) $\text{ZnBq}/\text{Ce6@ZIF-8@OMV}$ (40 $\mu\text{g}/\text{ml}$, contain $\text{Zn}(\text{Bq})_2 \sim 0.44 \mu\text{g}/\text{ml}$) + light. (F) Bacterial tube killing rate under different treatments: (i) control, (ii) Bq (1 $\mu\text{g}/\text{ml}$), (iii) Zn(II) 50 μM , and (iv) $\text{Zn}(\text{Bq})_2$ (1.1 $\mu\text{g}/\text{ml}$). (G) Bacterial tube killing rate after 24-hour treatments of different groups: control, $\text{ZnBq}/\text{Ce6@ZIF-8}$ (40 $\mu\text{g}/\text{ml}$), $\text{ZnBq}/\text{Ce6@ZIF-8}$ (40 $\mu\text{g}/\text{ml}$) + light, $\text{ZnBq}/\text{Ce6@ZIF-8@OMV}$ (40 $\mu\text{g}/\text{ml}$), and $\text{ZnBq}/\text{Ce6@ZIF-8@OMV}$ (40 $\mu\text{g}/\text{ml}$) + light.

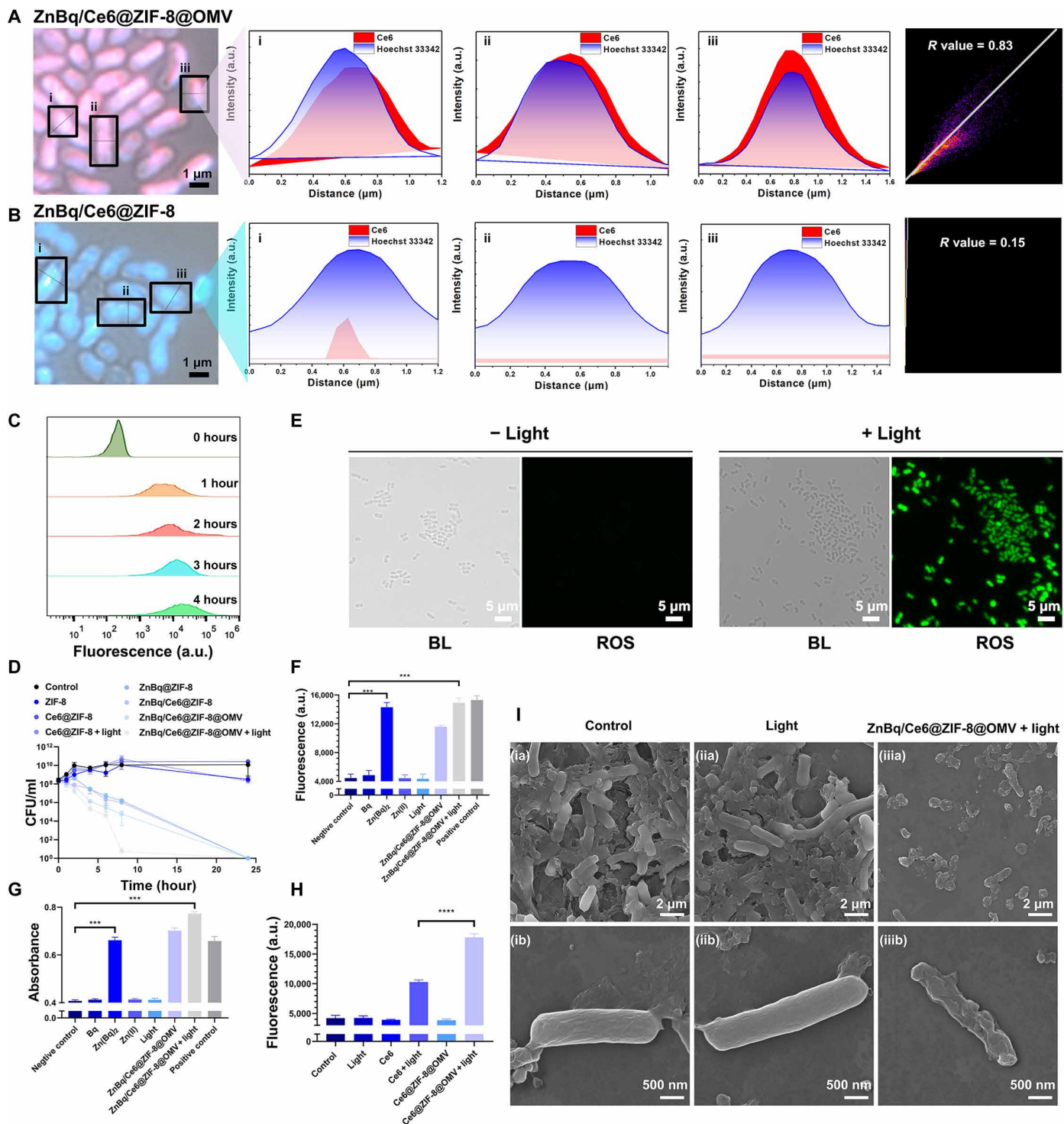


Fig. 5. Antibacterial mechanism of ZnBq/Ce6@ZIF-8@OMV. (A) Merged fluorescence image of ZnBq/Ce6@ZIF-8@OMV(20 $\mu\text{g/ml}$)–treated *A. baumannii* and the fluorescent colocalization in (i), (ii), and (iii) regions. (B) Merged fluorescence image of ZnBq/Ce6@ZIF-8(20 $\mu\text{g/ml}$)–treated *A. baumannii* and the fluorescent colocalization in (i), (ii) and (iii) regions. (C) Bacterial uptake analysis of ZnBq/Ce6@ZIF-8@OMV(40 $\mu\text{g/ml}$) by flow cytometry. (D) Bacterial killing rate under different treatments. (E) Detection of intrabacterial reactive oxygen species generation of ZnBq/Ce6@ZIF-8@OMV(20 $\mu\text{g/ml}$) by 2',7'-dichlorodihydrofluorescein diacetate staining. (F) Detection of the outer membrane under different treatments. (G) Detection of the inner membrane under different treatments. (H) Detection of the outer membrane under different treatments to verify the enhanced PDT. (I) SEM images of *A. baumannii* treated with PBS, light, and ZnBq/Ce6@ZIF-8@OMV(40 $\mu\text{g/ml}$) + light.

through classic NPN assay and ONPG assay. The NPN assay quantified the fluorescence value, providing an indication of the integrity of the outer membrane, while the ONPG assay measured the absorption value to assess the integrity of the inner membrane (as shown in Fig. 5, F and G). Our study demonstrated that the ZnBq/Ce6@ZIF-8@OMV + light group had the most potent effect in destroying both the inner and outer membranes of bacteria. This outcome can be attributed to two notable factors. First, the drug Zn(Bq)₂ itself has a destructive influence on the bacterial membranes (Fig. 5, F and G). Second, the targeting ability of OMV enabled the photosensitizer Ce6 to penetrate *A. baumannii* and induced more effective PDT, leading to further destruction of the bacterial membrane (Fig. 5H). Consequently, combining Zn(Bq)₂ chemotherapy with enhanced targeted PDT proved to be an effective strategy in the destruction of bacterial membranes. SEM and microscope imaging results further revealed that ZnBq/Ce6@ZIF-8@OMV was able to effectively kill bacteria and significantly alter their phenotype, destroying the membrane structure and thus causing serious bacterial death (Fig. 5I and fig. S34). Specifically, our findings suggest that the primary mechanism by which ZnBq/Ce6@ZIF-8@OMV caused bacterial death was through the destruction of the bacterial membrane structure after specifically targeting bacteria. To delve deeper into the antibacterial mechanism of Zn(Bq)₂, we conducted experiments to investigate its impact on DNA fragments. Our findings revealed that Zn(Bq)₂ did not exhibit any DNA fragment breakage and did not induce any DNA damage (fig. S35). In addition, we explored the influence of the ligand Bq on ferritin (fig. S36) and the tricarboxylic acid cycle (fig. S37), but no significant effects were observed. However, an intriguing discovery was made regarding the ability of Zn(Bq)₂ and Bq to lower the ATP levels in bacteria (fig. S38), highlighting their potential as agents capable of ATP reduction in bacteria. Nevertheless, investigating the specific mechanisms underlying this reduction in ATP levels still necessitates further exploration.

Biosafety of ZnBq/Ce6@ZIF-8@OMV

In vivo tests were also performed to inspect the efficacy of ZnBq/Ce6@ZIF-8@OMV. Before the in vivo therapeutic experiments, the biosafety of ZnBq/Ce6@ZIF-8@OMV was carefully inspected. It was found that ZnBq/Ce6@ZIF-8@OMV exhibited satisfactory cell safety (fig. S39), whereas the histological analysis of the major organs, such as the heart, liver, spleen, lung, and kidney, showed normal tissue morphology after ZnBq/Ce6@ZIF-8@OMV injection (fig. S40), demonstrating that ZnBq/Ce6@ZIF-8@OMV caused no overt tissue damage. In addition, blood biochemical analysis was conducted at 14 days after intravenous injection (fig. S41), demonstrating the minimal changes as compared to that of the control group.

In vivo eradication of *A. baumannii*-infected meningitis

It is well known that *A. baumannii*-infected meningitis was associated with a high fatality rate, particularly for immunocompromised patients. In this study, we pioneered a bacterial meningitis model and therapeutic protocol for *A. baumannii* (Fig. 6A). The in vivo targeting ability of ZnBq/Ce6@ZIF-8@OMV was compared with that of uncoated nanoparticles and large-size (fig. S42) MOF nanoparticles. Our results demonstrated that ZnBq/Ce6@ZIF-8@OMV had significantly higher and longer accumulation in the *A. baumannii*-infected brain as compared to that of the control groups (Fig. 6, B and C). In particular, the small-size ZnBq/Ce6@ZIF-8@OMV was

able to target the brain lesion areas more efficiently than large-sized MOF nanoparticles. Then, the BALB/c mice were randomly assigned to four treatment groups: (i) saline, (ii) laser irradiation (660 nm, 0.4 W/cm², 4 min), (iii) ZnBq/Ce6@ZIF-8@OMV (5 mg/kg), and (iv) ZnBq/Ce6@ZIF-8@OMV with laser irradiation (5 mg/kg, 660 nm, 0.4 W/cm², 4 min). Treatments were carried out 1 day after bacterial infection surgery. Laser speckle imaging was used to monitor the changes in cerebral cortical blood flow during the progression of meningitis (Fig. 6D). We found that cerebral blood flow significantly decreased on the right hemisphere of the brain 1 day after bacterial infection. However, for the group treated with ZnBq/Ce6@ZIF-8@OMV and light irradiation, microvessels gradually regenerated, cerebral blood flow gradually increased, and cortical lesion volume was significantly reduced (Fig. 6D). These changes indicated the treatment was highly effective in promoting recovery from the infectious disease. Moreover, the cured mice generated no significant change in brain tissue texture by hematoxylin and eosin staining and Gram-positive staining (fig. S43) and no tissue damage in organs including the heart, liver, spleen, lung, and kidney (fig. S44). We then performed Gram staining and serial dilution coating counting on homogenized infected brain tissue, so as to determine the effect of ZnBq/Ce6@ZIF-8@OMV with light irradiation treatment on bacterial load. Our results showed that this treatment markedly reduced the bacterial load, resulting in approximately 100-fold fewer bacteria in the mouse brain tissue as compared to that of nontreated groups (Fig. 6E). Moreover, in the treatment groups (light + drug), tumor necrosis factor- α levels exhibited a significant decrease when compared to the untreated group (fig. S45), approaching levels comparable to those in the healthy mice group. The significantly decreased bacterial distribution and prolonged survival time (Fig. 6F) demonstrated that ZnBq/Ce6@ZIF-8@OMV nanoplateforms lead to effective recovery from *A. baumannii* infection.

Evaluation of drug resistance of *A. baumannii* bacteria

More specifically, serial passage of *A. baumannii* in the presence of sub-MICs of Bq and ZnBq/Ce6@ZIF-8@OMV for 30 days was investigated to assess the development of resistant mutants (Fig. 6G). Exposure to sub-MIC concentrations over long periods of time might cause long-term adversity in bacteria, increase the frequency of genetic mutations, and enable the development of drug resistance (47). Bacteria exposed to sub-MIC concentrations of drug for a prolonged period will activate relevant pathways such as the SOS response, leading to increased genetic mutation frequency and drug resistance. Here, for norfloxacin as a DNA damage antibiotic, it was found that the highest concentration was 256 times the MIC, which indicated that the use of norfloxacin as an antibiotic may lead to the emergence of resistant bacterial strains. In this study, compared to the traditional antibiotic norfloxacin that was with a fourfold increase in MIC concentration after three generations of sub-MIC passage, the single-clone bacteria extracted after 30 generations of sub-MIC passage with ZnBq/Ce6@ZIF-8@OMV maintained the same MIC concentration and produced no drug-resistant mutants. Therefore, the bacterial killing of ZnBq/Ce6@ZIF-8@OMV is stable and not prone to drug resistance. Moreover, ZnBq/Ce6@ZIF-8@OMV + light treatment group remained at their original MIC, demonstrating the sustained bactericidal activity with ZnBq/Ce6@ZIF-8@OMV and reducing the risk of bacteria developing resistance to them. These findings indicate that ZnBq/Ce6@ZIF-8@OMV manifested excellent killing stability and showed the potential long-term

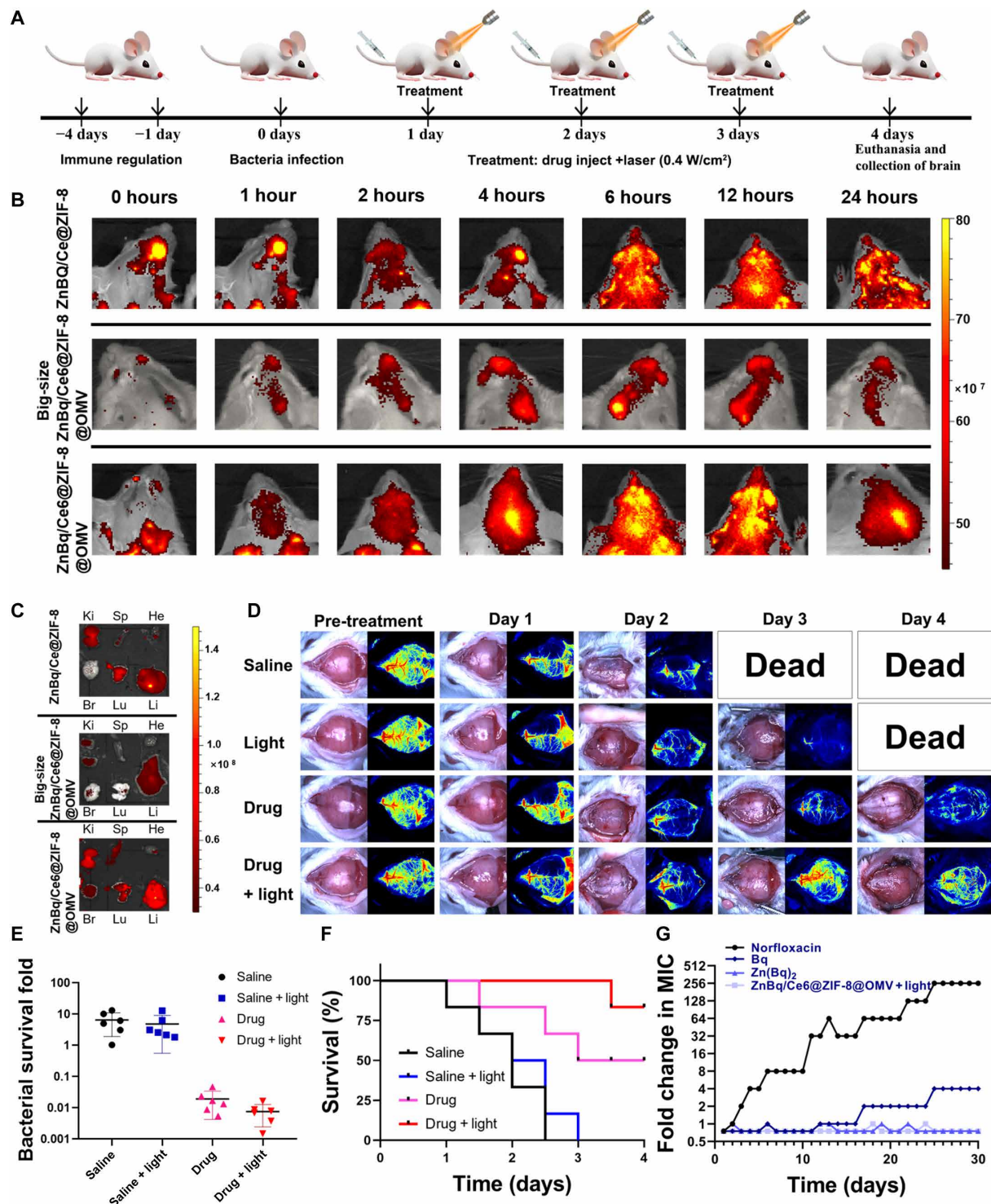


Fig. 6. Antibacterial effects of ZnBq/Ce6@ZIF-8@OMV in vivo. (A) Schematic of the construction and treatment process of meningitis infection. (B) Representative in vivo fluorescence imaging of BALB/c mice treated with ZnBq/Ce6@ZIF-8, large-size ZnBq/Ce6@ZIF-8@OMV, and ZnBq/Ce6@ZIF-8@OMV at 0, 1, 2, 4, 6, 12, and 24 hours. (C) Ex vivo fluorescence images of major organs at 24 hours were shown. (D) In vivo photoacoustic imaging of meningitis mice with different treatment groups. (E) Bacteria content analysis of the brain tissue for different treatment groups. (F) Survival curves of infected BALB/c mice for various treatment groups. (G) Drug resistance assessment for different treatment groups.

efficacy and stability of drugs in combating *A. baumannii* infections and reducing the development of drug-resistant strains.

DISCUSSION

In recent decades, the excessive use of antibiotics has resulted in the emergence and widespread dissemination of MDRB, posing a notable challenge to public health (48). Among these MDRB, some have been classified by the WHO as ESKAPE pathogens, demanding priority attention (49). One such pathogen is multidrug-resistant *A. baumannii* bacteria. Sadly, the limited availability of effective antibiotics for treating *A. baumannii* bacterial infections leaves health care professionals with only a handful of options, known as the last line of defense—such as tigecycline and colistin (4, 50). Nevertheless, it is crucial to acknowledge that these antibiotics come with adverse effects, including kidney toxicity, and the emergence of resistant strains to tigecycline and colistin has already been reported (27, 28, 51). Consequently, the dire situation of antibiotic scarcity calls for immediate action in developing new antibiotics. Here, we have made substantial progress in our research by identifying a small molecule drug, Bq, that effectively kills *A. baumannii* bacteria (MIC of approximately 2 $\mu\text{g}/\text{ml}$). Moreover, we have further optimized its antibacterial efficacy by creating a $\text{Zn}(\text{Bq})_2$ metal complex, which displayed an impressive MIC value of 0.21 $\mu\text{g}/\text{ml}$, lower than most of the recently developed antimicrobial agents (normally >4 $\mu\text{g}/\text{ml}$) (52–55), even lower than the MIC value (2 $\mu\text{g}/\text{ml}$) of the drug recently screened out by deep learning (56). Furthermore, extensive passage experiments carried out on $\text{Zn}(\text{Bq})_2$ and $\text{ZnBq}/\text{Ce6@ZIF-8@OMV}$ have provided compelling evidence that it maintains a consistently potent bactericidal efficacy, even after a prolonged period of 30 days (Fig. 6G), without succumbing to the development of resistance, which is apart from traditional antibiotics such as colistin (often considered as a last resort treatment option), which have already encountered resistant mechanisms such as the MCR-1 gene (7). It exhibits a prolonged period of efficacy (30 days) without developing resistance, surpassing the typical resistance life span observed in found drugs (typically less than 20 days or cycles) (57, 58). The extraordinary bactericidal efficacy and exceptional killing stability exhibited by $\text{Zn}(\text{Bq})_2$ make it a superior alternative to conventional antibiotics like colistin, which face increasing challenges in treating resistant *A. baumannii* infections.

In addition, we have made notable advancements in the field of bacteria targeting. By leveraging cutting-edge genetic engineering technology, we have successfully engineered an OMV structure that expresses bacteria-targeting proteins (Fig. 3, N and O). These proteins effectively coat nanoscale MOF, enabling precise and targeted therapy against specific bacteria. This innovative targeting strategy brings about several notable advantages. First, it allows for the reduction of drug concentration required for treatment with the antibacterial $\text{Zn}(\text{Bq})_2$. Consequently, the toxicity and side effects associated with the drug are minimized. Moreover, by specifically targeting bacteria, this strategy enables faster antibacterial action, accelerating the rate of bacterial elimination (Fig. 5D). In addition, our approach to targeted bacterial treatment significantly enhances the effectiveness of PDT antibacterial methods. PDT produces a lethal ROS with high oxidation ability. Nevertheless, note that the action radius of PDT is typically limited (59), with a radius of action for singlet oxygen of less than 1 μm , and even smaller for highly reactive hydroxyl radicals. Therefore, establishing close spatial proximity between

photosensitizers and target bacteria is indispensable to unleash the full potential of ROS on bacterial components. By leveraging the bioengineered membrane-based antibacterial strategy, we are able to generate specific targeted bacterial membranes (Fig. 5A), significantly amplifying the bactericidal effects of PDT (Fig. 5H). Overall, this pioneering strategy of using bioengineered OMV membrane for specific targeted antibacterial activities holds immense potential for improving the efficacy of various antibacterial drugs.

To ensure the proper delivery of the $\text{Zn}(\text{Bq})_2$ metal complex, we have developed a transport system based on the utilization of ZIF-8 (forming $\text{ZnBq}/\text{Ce6@ZIF-8}$, Fig. 3). Unlike traditional MOF characterized by large sizes (providing large enough pore size to load metal complex) (46, 60) that pose limitations in transporting this metal complex for in vivo bioapplications, we have exclusively used nano-sized ZIF-8 to transport the metal complex. By using nano-sized MOFs for this synthesis process, we can target specific sites more effectively, as large-sized MOFs would undergo metabolic processes within the bloodstream due to their large size. This advancement has also paved the way for the practical application of metal complexes and MOF in drug loading. It is crucial to highlight the importance of carefully selecting the appropriate type of MOF for drug loading as our system (Fig. 2G) indicated that copper- or iron-based MOF (may generate Cu^{2+} , Fe^{2+} , and Fe^{3+} ions) will fail to achieve the desired antibacterial effect when loaded with Bq.

This paper provides empirical evidence supporting the significant antibacterial efficacy of the chosen $\text{Zn}(\text{Bq})_2$ compound. However, a comprehensive understanding of its underlying antibacterial mechanism necessitates further investigation. Previous studies have provided indications of the antibacterial properties exhibited by metal complexes with comparable structures, which resulted in observable damage to the bacterial cell wall (61); however, a thorough examination of the associated mechanisms remains limited. Our study also affirmed that the antibacterial mechanism primarily emerges from the disruption caused by $\text{Zn}(\text{Bq})_2$ on both the inner and outer bacterial membranes (Fig. 5, F and G). This bactericidal effect may stem from the coordination capabilities of metal ions with Bq, although the precise path of this destructive process requires additional in-depth scrutiny.

Overall, our research has made notable strides in addressing the limitations of antibiotics against *A. baumannii* bacteria. The integration of $\text{Zn}(\text{Bq})_2$ metal complex and Ce6, along with the tailored transport system based on nano-sized ZIF-8, has generated promising antibacterial outcomes in vitro. Furthermore, by coating OMV, the bacterial-specific biomimetic nanodrugs strongly disrupted *A. baumannii*-infected biofilm (Fig. 4E) and rapidly promoted the mice meningitis healing (Fig. 6D). We hope that this novel approach will contribute to being translated into clinical applications for treatment of various *A. baumannii*-induced diseases in the future.

METHODS

Bacterial strains and growth conditions

The bacterial strains and plasmids used in this study are listed in Table 1. LB broth, Miller (Luria-Bertani) (BD Biosciences, 244620) was used for all the experiments.

Plasmid and bacterial strains construction

In this study, the pBAD_ *clyA*-antiBap plasmid was constructed by In-Fusion Cloning (TaKaRa, 638943). pBAD was lined by restriction

Table 1. List of strains used in the study.

Strain	Application
<i>A. baumannii</i> ATCC 19606	Compound library screening, checkerboard assay, killing assay, animal infection, and uptake assay
<i>A. baumannii</i> ATCC 17978	Checkerboard assay and killing assay
<i>A. baumannii</i> ATCC 1800	Checkerboard assay and killing assay
<i>E. coli</i> MG1655 Δ <i>msbB</i>	Protein expression and OMV extraction
<i>E. coli</i> MG1655	Mutant construction
<i>E. coli</i> MFD λ pir	Mutant construction
<i>E. coli</i> DH5 α λ pir	Mutant construction and plasmid construction

enzymes NcoI as well as PstI. The *clyA* fragment and antiBap fragment were amplified using primers from Table 2. In-frame deletion mutant Δ *msbB* was constructed on the basis of SacB-mediated allelic exchange with suicide plasmid pDS132 as described previously (62). *E. coli* MG1655 was used as the parental strain. Briefly, the primers (Table 2) were used to amplify the upstream and downstream flanking sequence of *msbB*. The resultant polymerase chain reaction (PCR) products that included fragments containing 792 bp of the upstream and downstream of *msbB* were cloned into pDS132 plasmid after being digested by the restriction enzymes XbaI, which were further transferred into *E. coli* MFD λ pir and conjugated with MG1655. Double cross-over deletion mutants were obtained and verified by PCR.

Bacterial OMV-antiBap and extracellular vesicle preparation

OMV-antiBap was prepared in Δ *msbB* (pBAD-*clyA*-antiBap) strain following the OMV preparation protocol described previously (30). Briefly, colonies of bacteria from the LB Agar were picked up and then put in 20 ml of LB, 37°C, 220 rpm overnight. Then, they were diluted by the ratio of 1:100 into fresh LB (BD Biosciences, 244620), followed by being cultured until optical density (OD₆₀₀) between 0.5 and 0.55 (i.e., exponential phase). Arabinose (0.1%; diluted 1:200 in LB broth) was added to induce the expression of ClyA-antiBap-flag protein. After being incubated overnight at 37°C with shaking (220 rpm), the bacteria were centrifuged at 8000g for 10 min. The supernatant was passed through a 0.45- μ m polyvinylidene fluoride filter (Millipore, R8SA47939, USA) and concentrated to 2 ml using 100-kDa ultrafiltration membranes (Millipore, R3EA06699, USA). The concentration was filtered with a 0.22- μ m filter to mitigate any contamination and then stored at -20 °C until use. The total protein concentration was quantified using the NanoDrop (Thermo Fisher Scientific, USA) and bicinchoninic acid protein assay.

Compound library screening

Compound library screening was performed based on the previous protocol with minor modifications (63). The FDA-approved drug screening library (Selleck, L1300_Z83049) includes about 1100 chemical compounds from Selleck Chemicals. Briefly, *A. baumannii* ATCC 19606 was cultured in LB broth at 37°C overnight, which was then diluted 1:100 into 3 ml fresh Difco LB broth, Miller (Luria-Bertani) (BD Biosciences, 244620). The culture was grown until the optical density (OD₆₀₀) reached between 0.5 and 0.55,

which corresponded to the exponential phase of growth. Bacteria were then diluted to OD₆₀₀ = 0.05 by fresh LB. One hundred microliters of bacterial culture was added to each well of the 96-well plate, which contained a 40 μ M compound. The plates were kept at 37°C for 16 hours and the OD₆₀₀ value was recorded using a SpectraMax M5 multi-detection microplate reader system (Molecular Devices, San Jose, CA, USA). Compounds that resulted in bacterial OD₆₀₀ smaller than 0.1 were considered as the potential anti-bacterial drug.

Resistance analysis

Resistance development was studied by sequential passaging following the previous protocol (47). Bacteria cells at the mid-log phase were diluted to an OD₆₀₀ of 0.01. LB with Bq, zinc, photoirradiated nanoplast, or norfloxacin was shakingly incubated at 37°C, and then passaged every 24 hours in the presence of Bq, zinc, or norfloxacin at subinhibitory concentration. The final value of OD₆₀₀ was measured by the Tecan Infinite M200 PRO multifunctional microplate reader. Experiments were performed with biological replicates.

Preparation of Zn(Bq)₂

The Zn(Bq)₂ compound was synthesized using the following procedure. First, 1 mmol of Zn (Aladdin, Z111245) and 2 mmol of Bq were accurately weighed and dissolved in 40 ml of *N,N'*-dimethylformamide (DMF). The mixture was allowed to react for 10 min. Subsequently, 20 ml of water was added to the reaction mixtures, followed by centrifugation for 10 min at 8500 rpm. The resulting mixture was then dried at 60°C, resulting in the formation of yellow Zn(Bq)₂ powder.

Preparation of ZnBq/Ce6@ZIF-8@OMV nanoparticles

Zinc acetate (0.35 g; Aladdin, Z111245) and 2.5 g of 2-methylimidazole (Aladdin, M104839) were dissolved in 10 ml of deionized water. Twenty milligrams of Bq was dissolved in 10 ml of DMF. Aqueous zinc acetate (1.7 ml) was mixed with 3 ml of DMF for 3 min. Eight hundred microliters of Bq or Ce6 was mixed and stirred vigorously at room temperature. Then, 4 ml of 2-methylimidazole was mixed and stirred constantly for 30 min. The product was collected by washing three times with deionized water and vacuum-drying. The OMV-antiBap with ZnBq/Ce6@ZIF-8 was extruded through a polycarbonate membrane with 100-nm pore size to yield ZnBq/Ce6@ZIF-8@OMV. The loading capacity was measured by using ultraviolet-visible (UV-vis) absorption spectra and the pH-responsive release of Ce6

Table 2. Primer's sequence.

Primer Name	Sequence (5'-3')
IDE1msbb.for	gatctgaactatgccctgctg
IDE1msbb.rev	taaacccgctgacgcaaaa
IDE2msbb.for	gtctggtgacctggtgattg
IDE2msbb.rev	aaaccgacacatgaccgt
msbbdown.for	aactggtcggcattcagaaa
msbbdown.rev	aaaagcctctcgcgaggaga
msbbup.for	gctttccagtttcggataa
msbbup.rev	gcagtggcaaatggattcc
cmbadhlyeF.FOR	aggaggaattcacatgatgactgaaatcgttgagat
cmbadhlyeF.REV	agccaagcttgatgcctactgcagcttgcctctttagtcgactcaggtacctcaaa-gagtg
cflag ab.for	agacgatgacgacaagctgcaggggtggtggtgtagt
cflag ab.rev	aaaacagccaagctttactgtcgtcatcgtctttagtagt

and Bq from ZIF-8 was studied through the absorbance in neutral and acid conditions.

Characterization of ZnBq/Ce6@ZIF-8@OMV nanoparticles

Absorption spectra were obtained by a UV-3101 spectrophotometer. TEM images were obtained by using Tecnai G2 F20 S-Twin at an acceleration voltage of 200 kV. The elemental mapping analysis used Tecnai F20 S-Twin electron microscopy. PXRD patterns were analyzed on a Bruker D8 Advance diffractometer using Cu-K α radiation ($\lambda = 1.54 \text{ \AA}$) from 10° to 90° in steps of $10^\circ/\text{min}$. The XPS spectra were recorded by an x-ray photoelectron Thermo Fisher Scientific ESCAL-AB 250Xi spectrometer. N₂ absorption-desorption isotherms were analyzed using Micromeritics ASAP 2460. A laser speckle imaging system was used to monitor animal meningitis. Bio-imaging analysis in vivo was performed using the IVIS Lumina XR system. Confocal laser scanning microscopy images were measured through a Nikon A1R confocal system.

Animal infection model

Mice were infected with *A. baumannii* ATCC 19606 in the brain. Briefly, neutropenic mice were induced by intraperitoneal administration of cyclophosphamide, with two doses given at 4 to 8 weeks before surgery (150 mg/kg) and 1 day before surgery (75 mg/kg) (64). The mice were intracranially inoculated in a cerebellomedullar cistern with 5 μl of *A. baumannii* suspension (10^6 CFU/ml). At 24 hours after surgery, mice were randomly separated into four groups ($n = 6$): control group, light group, drug group, and drug with light group. BALB/c mice were treated with repeated tail vein injections of (i) saline, (ii) light (660 nm, 0.4 W/cm², 4 min), (iii) ZnBq/Ce6@ZIF-8@OMV (5 mg/kg), and (iv) ZnBq/Ce6@ZIF-8@OMV + light (5 mg/kg, 660 nm, 0.4 W/cm², 4 min). Treatments were administered every 12 hours and lasted for 3 days. At 24 hours after the last treatment, mice were euthanized, and the intact brain was removed for homogenization in 1 ml of sterile 1 \times phosphate-buffered saline or paraffin slices after cardiac perfusion. Homogenates were subjected to 10-fold serial dilution and 100- μl samples of each dilution were spread onto LB agar plate for the enumeration of bacterial survivors. The animal experiments were approved by the Panel on Research Ethics of University of Macau (UMARE- 033-2020).

Supplementary Materials

This PDF file includes:

Supplementary Text

Figs. S1 to S45

Table S1

REFERENCE AND NOTES

1. D. L. Zimble, W. F. Penwell, J. A. Gaddy, S. M. Menke, A. P. Tomaras, P. L. Connerly, L. A. Actis, Iron acquisition functions expressed by the human pathogen *Acinetobacter baumannii*. *Biometals* **22**, 23–32 (2009).
2. D. Landman, J. M. Quale, D. Mayorga, A. Adedeji, K. Vangala, J. Ravishankar, C. Flores, S. Brooks, Citywide clonal outbreak of multiresistant *Acinetobacter baumannii* and *Pseudomonas aeruginosa* in Brooklyn, NY: The preantibiotic era has returned. *Arch. Intern. Med.* **162**, 1515–1520 (2002).
3. C. Ayoub Moubarek, D. Hammoudi Halat, Insights into *Acinetobacter baumannii*: A review of microbiological, virulence, and resistance traits in a threatening nosocomial pathogen. *Antibiotics* **9**, 119 (2020).
4. A. Y. Peleg, H. Seifert, D. L. Paterson, *Acinetobacter baumannii*: Emergence of a successful pathogen. *Clin. Microbiol. Rev.* **21**, 538–582 (2008).
5. J. Shi, T. Sun, Y. Cui, C. Wang, F. Wang, Y. Zhou, H. Miao, Y. Shan, Y. Zhang, Multidrug resistant and extensively drug resistant *Acinetobacter baumannii* hospital infection associated with high mortality: A retrospective study in the pediatric intensive care unit. *BMC Infect. Dis.* **20**, 597 (2020).
6. J. Brauers, U. Frank, M. Kresken, A. C. Rodloff, H. Seifert, Activities of various beta-lactams and beta-lactam/beta-lactamase inhibitor combinations against *Acinetobacter baumannii* and *Acinetobacter* DNA group 3 strains. *Clin. Microbiol. Infect.* **11**, 24–30 (2005).
7. J. Li, R. L. Nation, J. D. Turnidge, R. W. Milne, K. Coulthard, C. R. Rayner, D. L. Paterson, Colistin: The re-emerging antibiotic for multidrug-resistant Gram-negative bacterial infections. *Lancet Infect. Dis.* **6**, 589–601 (2006).
8. S. Lax, N. Sangwan, D. Smith, P. Larsen, K. M. Handley, M. Richardson, K. Guyton, M. Krezalek, B. D. Shogan, J. Defazio, I. Fleming, B. Shakhsheer, S. Weber, E. Landon, S. Garcia-Houchins, J. Siegel, J. Alverdy, R. Knight, B. Stephens, J. A. Gilbert, Bacterial colonization and succession in a newly opened hospital. *Sci. Transl. Med.* **9**, (2017).
9. C. Larson, Pharmaceuticals. China's lakes of pig manure spawn antibiotic resistance. *Science* **347**, 704 (2015).
10. D. van de Beek, M. Brouwer, R. Hasbun, U. Koedel, C. G. Whitney, E. Wijdicks, Community-acquired bacterial meningitis. *Nat. Rev. Dis. Primers.* **2**, 16074 (2016).
11. L. E. Davis, Acute bacterial meningitis. *CONTIN. Lifelong Learn. Neurol.* **24**, 1264–1283 (2018).
12. C. R. Lee, J. H. Lee, M. Park, K. S. Park, I. K. Bae, Y. B. Kim, C.-J. Cha, B. C. Jeong, S. H. Lee, Biology of *Acinetobacter baumannii*: Pathogenesis, antibiotic resistance mechanisms, and prospective treatment options. *Front. Cell. Infect. Microbiol.* **7**, 55 (2017).
13. L. C. Antunes, P. Visca, K. J. Townner, *Acinetobacter baumannii*: Evolution of a global pathogen. *Pathog. Dis.* **71**, 292–301 (2014).

14. R. Xie, X. D. Zhang, Q. Zhao, B. Peng, J. Zheng, Analysis of global prevalence of antibiotic resistance in *Acinetobacter baumannii* infections disclosed a faster increase in OECD countries. *Emerg. Microbes Infect.* **7**, 31 (2018).
15. World Health Organization, *2021 Antibacterial Agents in Clinical and Preclinical Development: An Overview and Analysis* (World Health Organization, 2022).
16. A. Frei, A. D. Verderosa, A. G. Elliott, J. Zuegg, M. A. T. Blaskovich, Metals to combat antimicrobial resistance. *Nat. Rev. Chem.* **7**, 202–224 (2023).
17. A. Pandey, E. Boros, Coordination complexes to combat bacterial infections: Recent developments, current directions and future opportunities. *Chem. - Eur. J.* **27**, 7340–7350 (2021).
18. A. Frei, Metal complexes, an untapped source of antibiotic potential? *Antibiotics* **9**, 90 (2020).
19. A. Frei, A. G. Elliott, A. Kan, H. Dinh, S. Bräse, A. E. Bruce, M. R. Bruce, F. Chen, D. Humaidy, N. Jung, A. P. King, P. G. Lyne, H. K. Maliszewska, A. M. Mansour, D. Matiadis, M. P. Muñoz, T. Y. Pai, S. Pokhrel, P. J. Sadler, M. Sagnou, M. Taylor, J. J. Wilson, D. Woods, J. Zuegg, W. Meyer, A. K. Cain, M. A. Cooper, M. A. T. Blaskovich, Metal complexes as antifungals? From a crowd-sourced compound library to the first in vivo experiments. *JACS Au*, **2**, 2277–2294 (2022).
20. F. Lovering, Escape from Flatland 2: Complexity and promiscuity. *MedChemComm* **4**, 515 (2013).
21. A. Frei, J. Zuegg, A. G. Elliott, M. Baker, S. Braese, C. Brown, F. Chen, C. G. Dowson, G. Dujardin, N. Jung, A. P. King, A. M. Mansour, M. Massi, J. Moat, H. A. Mohamed, A. K. Renfrew, P. J. Rutledge, P. J. Sadler, M. H. Todd, C. E. Willans, J. J. Wilson, M. A. Cooper, M. A. T. Blaskovich, Metal complexes as a promising source for new antibiotics. *Chem. Sci.* **11**, 2627–2639 (2019).
22. D. Du, X. Wang-Kan, A. Neuberger, H. W. van Veen, K. M. Pos, L. J. V. Piddock, B. F. Luisi, Multidrug efflux pumps: Structure, function and regulation. *Nat. Rev. Microbiol.* **16**, 523–539 (2018).
23. F. Li, J. G. Collins, F. R. Keene, Ruthenium complexes as antimicrobial agents. *Chem. Soc. Rev.* **44**, 2529–2542 (2015).
24. S. Yuan, Y. Zhu, Y. Dai, Y. Wang, D. Jin, M. Liu, L. Tang, F. Arnesano, G. Natile, Y. Liu, (19) f nmr allows the investigation of the fate of platinum(IV) prodrugs in physiological conditions. *Angew. Chem. Int. Ed. Engl.* **61**, e202114250 (2022).
25. J. C. Pessoa, I. Tomaz, Transport of therapeutic vanadium and ruthenium complexes by blood plasma components. *Curr. Med. Chem.* **17**, 3701–3738 (2010).
26. N.-H. Le, K. Peters, A. Espallat, J. R. Sheldon, J. Gray, G. D. Venanzio, J. Lopez, B. Djahanschiri, E. A. Mueller, S. W. Hennon, P. A. Levin, I. Ebersberger, E. P. Skaar, F. Cava, W. Vollmer, M. F. Feldman, Peptidoglycan editing provides immunity to *Acinetobacter baumannii* during bacterial warfare. *Sci. Adv.* **6**, eabb5614 (2020).
27. Y. P. Di, Q. Lin, C. Chen, R. C. Montelaro, Y. Doi, B. Deslouches, Enhanced therapeutic index of an antimicrobial peptide in mice by increasing safety and activity against multidrug-resistant bacteria. *Sci. Adv.* **6**, eaay6817 (2020).
28. Y. Fan, X. D. Li, P. P. He, X. X. Hu, K. Zhang, J. Q. Fan, P. P. Yang, H. Y. Zheng, W. Tian, Z. M. Chen, L. Ji, H. Wang, L. Wang, A biomimetic peptide recognizes and traps bacteria in vivo as human defensin-6. *Sci. Adv.* **6**, eaaz4767 (2020).
29. R. H. Fang, A. V. Kroll, W. Gao, L. Zhang, Cell membrane coating nanotechnology. *Adv. Mater.* **30**, e1706759 (2018).
30. Y. Li, R. Zhao, K. Cheng, K. Zhang, Y. Wang, Y. Zhang, Y. Li, G. Liu, J. Xu, J. Xu, G. J. Anderson, J. Shi, L. Ren, X. Zhao, G. Nie, Bacterial Outer membrane vesicles presenting programmed death 1 for improved cancer immunotherapy via immune activation and checkpoint inhibition. *ACS Nano* **14**, 16698–16711 (2020).
31. Q. Zhuang, J. Xu, D. Deng, T. Chao, J. Li, R. Zhang, R. Peng, Z. Liu, Bacteria-derived membrane vesicles to advance targeted photothermal tumor ablation. *Biomaterials* **268**, 120550 (2021).
32. R. H. Fang, W. Gao, L. Zhang, Targeting drugs to tumours using cell membrane-coated nanoparticles. *Nat. Rev. Clin. Oncol.* **20**, 33–48 (2023).
33. Y. Song, X. Zheng, J. Hu, S. Ma, K. Li, J. Chen, X. Xu, X. Lu, X. Wang, Recent advances of cell membrane-coated nanoparticles for therapy of bacterial infection. *Front. Microbiol.* **14**, 1083007 (2023).
34. T. M. Savage, R. L. Vincent, S. S. Rae, L. H. Huang, A. Ahn, K. Pu, F. Li, K. de los Santos-Alexis, C. Coker, T. Danino, N. Arpaia, Chemokines expressed by engineered bacteria recruit and orchestrate antitumor immunity. *Sci. Adv.* **9**, eadc9436 (2023).
35. C. R. Gurbatri, N. Arpaia, T. Danino, Engineering bacteria as interactive cancer therapies. *Science* **378**, 858–864 (2022).
36. Y. E. Chen, D. Bousbaine, A. Veinbachs, K. Atabakhsh, A. Dimas, V. K. Yu, A. Zhao, N. J. Enright, K. Nagashima, Y. Belkaid, M. A. Fischbach, Engineered skin bacteria induce antitumor T cell responses against melanoma. *Science* **380**, 203–210 (2023).
37. Z. Payandeh, I. Rasooli, S. L. Mousavi Gargari, M. Rajabi Bazl, W. Ebrahimzadeh, Immunoreaction of a recombinant nanobody from camelid single domain antibody fragment with *Acinetobacter baumannii*. *Trans. R. Soc. Trop. Med. Hyg.* **108**, 92–98 (2014).
38. H. Zheng, Y. Zhang, L. Liu, W. Wan, P. Guo, A. M. Nyström, X. Zou, One-pot synthesis of metal-organic frameworks with encapsulated target molecules and their applications for controlled drug delivery. *J. Am. Chem. Soc.* **138**, 962–968 (2016).
39. S. Kumari, T. S. Howlett, R. N. Ehrman, S. Koirala, O. Trashi, I. Trashi, Y. H. Wijesundara, J. J. Gassensmith, In vivo biocompatibility of ZIF-8 for slow release via intranasal administration. *Chem. Sci.* **14**, 5774–5782 (2023).
40. L. L. Merritt Jr., C. W. Weber, The solubilities of zinc complexes of 8-quinolinol and some derivatives of 8-quinolinol. *Talanta* **7**, 157–162 (1961).
41. D. C. Bhatnagar, L. S. Forster, The luminescence of oxines and metal oxinates. *Spectrochimica Acta* **21**, 1803–1807 (1965).
42. H. Jang, L.-M. Do, Y. Kim, T. Zyung, Y. Do, Synthesis and characterization of new luminescent materials containing various substituted 8-quinolinolate. *Synth. Met.* **121**, 1667–1668 (2001).
43. J. F. Toso, V. J. Gill, P. Hwu, F. M. Marincola, N. P. Restifo, D. J. Schwartzentruber, R. M. Sherry, S. L. Topalian, J. C. Yang, F. Stock, L. J. Freezer, K. E. Morton, C. Seipp, L. Haworth, S. Mavroukakis, D. White, S. MacDonald, J. Mao, M. Sznol, S. A. Rosenberg, Phase I study of the intravenous administration of attenuated *Salmonella typhimurium* to patients with metastatic melanoma. *J. Clin. Oncol.* **20**, 142–152 (2002).
44. X. Wei, M. Du, Z. Chen, Z. Yuan, Recent advances in bacteria-based cancer treatment. *Cancers* **14**, 4945 (2022).
45. V. Martínez, A. B. Gaspar, M. C. Muñoz, G. V. Bukin, G. Levchenko, J. A. Real, Synthesis and characterisation of a new series of bistable iron(II) spin-crossover 2D metal-organic frameworks. *Chemistry* **15**, 10960–10971 (2009).
46. Y. Zhang, H. Fu, S. Chen, B. Liu, W. Sun, H. Gao, Construction of an iridium(III)-complex-loaded MOF nanoplatfrom mediated with a dual-responsive polycationic polymer for photodynamic therapy and cell imaging. *Chem. Commun. (Camb.)* **56**, 762–765 (2020).
47. L. L. Ling, T. Schneider, A. J. Peoples, A. L. Spoering, I. Engels, B. P. Conlon, A. Mueller, T. F. Schäberle, D. E. Hughes, S. Epstein, M. Jones, L. Lazarides, V. A. Steadman, D. R. Cohen, C. R. Felix, K. A. Fetterman, W. P. Millett, A. G. Nitti, A. M. Zullo, C. Chen, K. Lewis, A new antibiotic kills pathogens without detectable resistance. *Nature* **517**, 455–459 (2015).
48. I. Levin-Reisman, I. Ronin, O. Gefen, I. Braniss, N. Shoshan, N. Q. Balaban, Antibiotic tolerance facilitates the evolution of resistance. *Science* **355**, 826–830 (2017).
49. R. Laxminarayan, D. Sridhar, M. Blaser, M. Wang, M. Woolhouse, Achieving global targets for antimicrobial resistance. *Science* **353**, 874–875 (2016).
50. C. J. Murray, K. S. Ikuta, F. Sharara, L. Swetschinski, G. R. Aguilar, A. Gray, C. Han, C. Bisignano, P. Rao, E. Wool, S. C. Johnson, Global burden of bacterial antimicrobial resistance in 2019: A systematic analysis. *Lancet* **399**, 629–655 (2022).
51. D. Nagarajan, N. Roy, O. Kulkarni, N. Nanajkar, A. Datey, S. Ravichandran, C. Thakur, I. V. Aprameya, S. P. Sarma, D. Chakravorty, N. Chandra, Ω 76: A designed antimicrobial peptide to combat carbapenem- and tigecycline-resistant *Acinetobacter baumannii*. *Sci. Adv.* **5**, eaax1946 (2019).
52. E. Jayathilaka, D. C. Rajapaksha, C. Nikapitiya, M. De Zoysa, I. Whang, Antimicrobial and anti-biofilm peptide octominin for controlling multidrug-resistant acinetobacter baumannii. *Int. J. Mol. Sci.* **22**, 5353 (2021).
53. D. Allison, E. Delancey, H. Ramey, C. Williams, Z. A. Alsharif, H. al-khattabi, A. Ontko, D. Gilmore, M. A. Alam, Synthesis and antimicrobial studies of novel derivatives of 4-(4-formyl-3-phenyl-1H-pyrazol-1-yl)benzoic acid as potent anti-*Acinetobacter baumannii* agents. *Bioorg. Med. Chem. Lett.* **27**, 387–392 (2017).
54. R. W. Deering, K. E. Whalen, I. Alvarez, K. Daffinee, M. Beganovic, K. L. LaPlante, S. Kishore, S. Zhao, B. Cezairliyan, S. Yu, M. Rosario, T. J. Mincer, D. C. Rowley, Identification of a bacteria-produced benzisoxazole with antibiotic activity against multi-drug resistant *Acinetobacter baumannii*. *J. Antibiot. (Tokyo)* **74**, 370–380 (2021).
55. A. Jahangiri, A. Neshani, S. A. Mirhosseini, G. Ghazvini, H. Zare, H. Sedighian, Synergistic effect of two antimicrobial peptides, Nisin and P10 with conventional antibiotics against extensively drug-resistant *Acinetobacter baumannii* and colistin-resistant *Pseudomonas aeruginosa* isolates. *Microb. Pathog.* **150**, 104700 (2021).
56. P. K. Hazam, C. C. Cheng, C. Y. Hsieh, W. C. Lin, P. H. Hsu, T. L. Chen, Y. T. Lee, J. Y. Chen, Development of bactericidal peptides against multidrug-resistant acinetobacter baumannii with enhanced stability and low toxicity. *Int. J. Mol. Sci.* **23**, 2191 (2022).
57. G. Liu, D. B. Catacutan, K. Rathod, K. Swanson, W. Jin, J. C. Mohammed, A. Chiappino-Pepe, S. A. Syed, M. Fragis, K. Rachwalski, J. Magolan, M. G. Surette, B. K. Coombes, T. Jaakkola, R. Barzilay, J. J. Collins, J. M. Stokes, Deep learning-guided discovery of an antibiotic targeting *Acinetobacter baumannii*. *Nat. Chem. Biol.* **19**, 1342–1350 (2023).
58. Y. M. Tan, Y. Wang, S. Li, S. L. Zhang, C. H. Zhou, Azolopyrimidinediols as novel structural scaffolds of DNA-Groove binders against intractable acinetobacter baumannii. *J. Med. Chem.* **66**, 4910–4931 (2023).
59. S. Gao, X. Yan, G. Xie, M. Zhu, X. Ju, P. J. Stang, Y. Tian, Z. Niu, Membrane intercalation-enhanced photodynamic inactivation of bacteria by a metallacycle and TAT-decorated virus coat protein. *Proc. Natl. Acad. Sci. U.S.A.* **116**, 23437–23443 (2019).
60. T. O. Knedel, S. Buss, I. Maisuls, C. G. Daniliuc, C. Schlüsener, P. Brandt, O. Weingart, A. Vollrath, C. Janiak, C. A. Strassert, Encapsulation of phosphorescent Pt(II) complexes in zn-based metal-organic frameworks toward oxygen-sensing porous materials. *Inorg. Chem.* **59**, 7252–7264 (2020).

61. B. R. Short, M. A. Vargas, J. C. Thomas, S. O'Hanlon, M. C. Enright, In vitro activity of a novel compound, the metal ion chelating agent AQ+, against clinical isolates of *Staphylococcus aureus*. *J. Antimicrob. Chemother.* **57**, 104–109 (2006).
62. J. Zheng, S. L. Tung, K. Y. Leung, Regulation of a type III and a putative secretion system in *Edwardsiella tarda* by EsrC is under the control of a two-component system, EsrA-EsrB. *Infect. Immun.* **73**, 4127–4137 (2005).
63. C. Lu, N. Zhang, S. Kou, L. Gao, B. Peng, Y. Dai, J. Zheng, Sanguinarine synergistically potentiates aminoglycoside-mediated bacterial killing. *J. Microbial. Biotechnol.* **15**, 2055–2070 (2022).
64. A. F. Zuluaga, B. E. Salazar, C. A. Rodriguez, A. X. Zapata, M. Agudelo, O. Vesga, Neutropenia induced in outbred mice by a simplified low-dose cyclophosphamide regimen: Characterization and applicability to diverse experimental models of infectious diseases. *BMC Infect. Dis.* **6**, 55 (2006).

Acknowledgments: We thank S. Qu, F. Zhang, F. Wu, X. Zhang, X. Wei, the Animal Research Core and Biological Imaging, and Stem Cell Core, Faculty of Health Sciences, University of Macau for assistance on this project. **Funding:** This work was also supported by the University of Macau (MYRG2020-00067-FHS, MYRG2019-00082-FHS, MYRG2022-00054-FHS and

MYRG-GRG2023-00038-FHS-UMDF), Macao Science and Technology Development Fund (FDCT 0020/2019/AMJ and FDCT 0048/2021/AGJ), and Higher Education Fund of Macao SAR Government Natural Science Foundation of Guangdong Province (EF017/FHS-YZ/2021/GDST). This work is also supported by the Shenzhen Science and Technology Program (grant no. ZDSYS20200811143600001). **Author contributions:** X.W., J.Z., and Z.Y. were involved in conceptualizing the project. X.W., B.X., S.R., J.Z., and Z.Y. contributed to the development of the methodology. The investigation was conducted by X.W., B.X., S.R., J.G., Y.H., X.G., and D.W. X.W., B.X., S.R., and C.Z. were responsible for visualizing the data. J.Z. and Z.Y. provided supervision throughout the project. The original draft of the manuscript was written by X.W., B.X., and S.R., while Z.Y. conducted the review and editing process. **Competing interests:** The authors declare that they have no competing interests. **Data and materials availability:** All data needed to evaluate the conclusions in the paper are present in the paper and/or the Supplementary Materials.

Submitted 1 September 2023

Accepted 16 February 2024

Published 22 March 2024

10.1126/sciadv.adk6331